ARTICLE

Flame Synthesis of Nanosized Cu−Ce−O, Ni−Ce−O, and Fe−Ce−O Catalysts for the Water-Gas Shift (WGS) Reaction

Ranjan K. Pati, Ivan C. Lee, Sicong Hou, Osifo Akhuemonkhan, Karen J. Gaskell, Qi Wang, Anatoly I. Frenkel, Deryn Chu, Lourdes G. Salamanca-Riba, and Sheryl H. Ehrman*

Department of Chemical and Biomolecular Engineering, University of Maryland, College Park, Maryland 20742, US Army Research Laboratory, Sensors and Electron Devices Directorate, Adelphi, Maryland 20783, Department of Chemistry and Biochemistry, University of Maryland, College Park, Maryland 20742, Department of Materials Science and Engineering, University of Maryland, College Park, Maryland 20742, and Department of Physics, Yeshiva University, New York, New York 10016

ABSTRACT A flame synthesis method has been used to prepare nanosized, high-surface-area Cu−Ce−O, Ni−Ce−O, and Fe−Ce−O catalysts from aqueous solutions of metal acetate precursors. The particles were formed by vaporization of the precursors followed by reaction and then gas to particle conversion. The specific surface areas of the synthesized powders ranged from 127 to 163 m^2/g. High-resolution transmission electron microscope imaging showed that the particle diameters for the ceria materials are in the range of 3−10 nm, and a thin layer of amorphous material was observed on the surface of the particles. The presence and surface enrichment of the transition-metal oxides (CuO, NiO, and Fe_2O_3) on the ceria particles were detected using X-ray photoelectron spectroscopy. Electron energy-loss spectroscopic studies suggest the formation of a core−shell structure in the as-prepared particles. Extended X-ray absorption fine structure studies suggest that the dopants in all M−Ce−O systems are almost isostructural with their oxide counterparts, indicating the doping materials form separate oxide phases (CuO, Fe_2O_3, NiO) within the host matrix (CeO_2). Etching results confirm that most of the transition-metal oxides are present on the surface of CeO_2, easily dissolved by nitric acid. The performance of the flame-synthesized catalysts was examined toward water-gas shift (WGS) activity for fuel processing applications. The WGS activity of metal ceria catalysts decreases in the order Cu−Ce−O > Ni−Ce−O > Fe−Ce−O > CeO_2 with a feed mixture having a hydrogen to carbon monoxide (H_2/CO) ratio of 1. There was no methane formation for these catalysts under the tested conditions.

KEYWORDS: WGS catalysts • nanoparticles • flame synthesis • transmission electron microscopy • X-ray photoelectron spectroscopy

1. INTRODUCTION

Ceria (CeO_2) is an important inorganic material having a cubic fluorite type crystal structure (1), which is stable from room temperature to its melting point (2673 K). Ceria either in the pure form or doped with other metals (Mg^{2+}, La^{2+}, Sc^{2+}, Gd^{3+}, Y^{3+}, Zr^{4+}, etc.) is of interest for a wide range of applications, including gas sensors (2), abrasives (3), electrode materials for solid oxide fuel cells (4), and three-way catalytic supports for automobile exhaust gas treatment (5, 6). Its performance as a solid electrolyte is close to that of ZrO_2, because of its high oxygen ion conductivity at comparatively low temperatures (7). The unique redox features of ceria, in particular the ability to shift between CeO_2 and CeO_{2-x} under reaction conditions, contribute to its success, especially when ceria is used as a component of the so-called three-way catalysts (8). Nonstoichiometric CeO_{2-x}-based nanocrystalline catalysts have been shown to provide excellent activity for SO_2 reduction by CO, CO oxidation, water-gas shift (WGS) reaction, and CH_4 oxidation (9−18).

Various solution-based techniques have been used for the preparation of pure ceria and transition-metal-doped ceria materials, which include coprecipitation (19−21), hydrothermal (22), microemulsion (23−25), sol−gel (26, 27), and solution combustion (28−30) methods. In addition, solid-state reaction and chemical vapor deposition (CVD) have also been used to make ceria-based materials (31, 32).

These methods involve multiple steps, are time-consuming (e.g. solution based techniques), or present difficult control of the product composition (e.g. CVD). In most of these methods, cerium oxide powders were formed with surface areas less than 100 m^2/g and only in a few cases were surface areas close to 200 m^2/g (23, 33). Generally, heat treatment at temperatures as low as 973 K is necessary to crystallize pure ceria, and this causes loss of surface area, a disadvantage of those synthesis methods. This drop in surface area can be partially reduced by doping with selected rare earth or transition metals (6). Additionally, doping with selected rare earth or transition metals can also boost the redox activity by promoting the formation of oxygen vacancies (34, 35). Over the past few years, aerosol technology

* To whom correspondence should be addressed. E-mail: sehrman@umd.edu. Tel: 1-301-405-1917. Fax: 1-301-405-0523.
Received for review August 11, 2009 and accepted October 22, 2009

DOI: 10.1021/am900533p

Published on Web 11/03/2009

has gained popularity for the synthesis of ceria with high surface area at high temperatures, as well as to make a variety of additional oxide nanoparticles (36). Suzuki et al. prepared polyhedral ceria nanoparticles of 50 nm in diameter by atomizing a 1 M cerium nitrate aqueous solution into fine droplets and reacting them in an argon inductively coupled plasma (37). Single-crystal ceria nanoparticles with surface area up to 250 m^2/g have been prepared by the inert gas condensation method (38). With a similar process using the inert gas condensation method, nanocrystalline La-doped CeO_{2-x} was prepared with a surface area of 80 m^2/g (39).

The flame synthesis method is a promising technique for the preparation of single (40) and mixed oxide (41, 42) powders. Mädler et al. prepared ceria nanoparticles (particle diameter less than 10 nm) by the flame synthesis method using cerium acetate dissolved in a mixture of acetic acid, 2-butanol, and isooctane (40). In this process, the presence of particles greater than 100 nm in diameter was due to the incomplete vaporization of the precursor droplets under optimal conditions. Particles below 10 nm are formed via precursor evaporation, ceria nucleation, and sintering of the particles. The use of isooctane in this process increased the flame temperature, enhancing precursor evaporation and reducing the formation of the residue.

In the present paper, we report a single-step flame synthesis process for the preparation of nanosized Cu−Ce−O, Ni−Ce−O, and Fe−Ce−O catalysts. The process involves the pyrolysis of aqueous solutions of metal acetate precursors in a premixed methane/oxygen/nitrogen flame without addition of any extra fuel. The results of surface characterization of the materials are given, and the arrangement of different atomic species in the catalysts is discussed. We also describe an investigation of the water-gas shift reaction over the Cu−Ce−O, Ni−Ce−O, and Fe−Ce−O catalysts to elucidate the catalytic properties of these flame-made ceria-based materials.

2. EXPERIMENTAL SECTION

The precursors used were cerium acetate (Strem Chemicals, 99.9%), copper acetate (Strem Chemicals, >98%), nickel acetate (Strem Chemicals, >98%), and iron acetate (Sigma-Aldrich Chemicals, >99.0%) as the cerium, copper, nickel, and iron sources, respectively. The precursors were dissolved in deionized water to make 0.3 M solutions of each. For the transition metal (M = Cu, Ni, Fe) supported ceria, a series of 0.3 M solutions were prepared with concentrations corresponding to metal to cerium (M:Ce) ratios of 5:95, 10:90, 15:85, 20:80, 25:75, 30:70, 40:60, 50:50, 60:40, 70:30, 80:20, 90:10, and 100:0. These ratios correspond to mole percent on a metals basis (mol % MB): for example, 5 mol % MB M−Ce−O for a M:Ce ratio of 5:95 and so on. The solutions were filtered through a membrane filter before being placed in the nebulizer (Gemini Scientific Corp., Inc.). In the nebulizer, the solutions were atomized with compressed air, having a flow rate of 4.0 L/min, resulting in a fine spray with a droplet mass median diameter in the range of 5.1 μm with a geometric standard deviation of 2.0 (43) that was fed into the flame reactor. The flow rate of the liquid precursor solution into the flame was 0.5 mL/min. In the reactor, the premixed flame was made by combining methane, oxygen, and nitrogen. The total flow rates for each gas, including the contributions from the air used to atomize the precursor, were methane 0.9 L/min, oxygen 2.6 L/min, and nitrogen 5.9 L/min. The flows of all gases were controlled by rotameters. The burner itself had an adjustable width slit geometry with a 19.5 cm long slit. The slit width used in these experiments was 0.3 cm. The maximum temperature of the flame using these flow rates was approximately 1773 K with a cooling rate of approximately 573 K/cm, which was measured using an S-type (Pt/10% Rh−Pt) thermocouple. The particles were collected by thermophoresis onto a water-cooled surface, which was positioned 2 cm above the top of the flame front and 6.5 cm above the top surface of the burner.

The synthesized materials were then characterized by powder X-ray diffraction (XRD, Bruker AXS D8 Advance) using Cu Kα (λ = 1.5408 Å) incident radiation for phase analysis and crystal structure determination. Thermogravimetric analysis (TGA, Perkin-Elmer Thermogravimetric Analyzer TGA-7) was used to determine the amount of unwanted materials such as water and carbonaceous compounds in the samples. Atomic bonding was analyzed using Fourier transform infrared spectroscopy (FTIR, Magna-IR 550 spectrometer). The Brunauer−Emmett−Teller (BET, Micromeritics ASAP 2010C) gas absorption method was applied to investigate the surface area of the samples. The particle diameter was calculated from BET surface area using the formula

$$D = 6/S\rho \quad (1)$$

where D is the particle diameter, S is the surface area, and ρ is the density of the material. The density was calculated according to the percentage of each oxide component present in the composition.

High-resolution transmission electron microscopic (HRTEM, JEOL 2100) imaging was used for the particle size analysis and surface morphology of the material. A JEOL JEM-2100FE transmission electron microscope equipped with a Gatan imaging filter (GIF) was used with an accelerating voltage of 200 kV and a probe diameter of 0.5 nm to study the electron energy loss spectra (EELS) of the as-prepared materials.

X-ray photoelectron spectra were collected on a Kratos Axis 165 X-ray photoelectron spectrometer operating in the hybrid mode using Al Kα X-radiation (1486.6 eV) at 300 W. Survey spectra were collected at a pass energy of 160 eV and high-resolution spectra at a pass energy of 40 eV. The charge neutralizer was used to minimize sample charging and was operated at 2.0 A current, 2.5 V charge balance, and 1.0 V bias; these values were optimized to give peaks with the narrowest FWHM (full width at half-maximum). Argon ion sputter profile data were collected at an argon pressure of $\sim 8 \times 10^{-8}$ Torr, with the gun operating at 4 kV and 5 mA, resulting in a current density of ~ 40 $\mu A/cm^2$. The beam was rastered, resulting in a crater of approximately 3 mm^2. Percentage atomic compositions were determined using CASA XPS software using RSF (relative sensitivity factors) obtained from the Kratos vision library.

To further investigate the surface enrichment, the as-prepared samples were immersed in 50 wt % dilute nitric acid solution for 24 h, filtered, and washed with deionized water thoroughly to remove any dissolved transition-metal oxide in the sample. Atomic absorption spectroscopic (AAS, Perkin-Elmer ICP-OES, Optima 5300 V) analysis of as-prepared M−Ce−O and etched M−Ce−O samples (M = Cu, Ni, Fe) was performed to identify the amount of transition metal present in both the as-prepared and etched samples and to estimate their relative amount on the surface as well as that dissolved in the ceria phase.

X-ray absorption spectroscopy (EXAFS) experiments were carried out at the beamline X18B of the National Synchrotron

Light Source (NSLS) at Brookhaven National Laboratory (BNL), Upton, NY. EXAFS analysis of the K-edge of doping elements M (M = Cu, 8979 eV; M = Fe, 7112 eV; M = Ni, 8333 eV) was done to characterize the local structures around M in the M−Ce−O system, while the L_3-edge EXAFS of Ce (5723 eV) was analyzed to determine the structure of the host matrix in the same system.

The reaction rates for WGS of Cu−Ce−O, Ni−Ce−O, and Fe−Ce−O catalysts were measured at atmospheric pressure with powder catalysts (9−11 mg) loaded at the center of a 0.6 cm tubular quartz reactor. The as prepared catalysts were used without activation. The typical catalyst bed length was 2 mm. The gas feed was a premixed 5 wt % CO and 5 wt % H_2, and the flow rate was controlled by MKS mass flow controllers. The reactor was open to the atmosphere, and the pressure drop was always less than 0.7×10^5 Pa to ensure that the change in reactant concentrations in the bed due to pressure effect was small. Water was injected into the flowing gas stream by a Shimadzu HPLC liquid pump and vaporized in a temperature-controlled Eppendorf column heater before entering the reactor. The water in the reactor exit stream was collected by an ice−water condenser. The conversion of all the reported measurements was less than 10 % so that we could assume differential conditions. The product gas stream was then analyzed on line simultaneously by two separation columns of an Agilent 3000 micro-gas chromatograph. A molecular sieve column (using argon as carrier gas) separated the carbon monoxide, hydrogen, and methane; a Plot U column (using helium as carrier gas) separates the carbon dioxide. The analysis of each injection took 3 min. Gas compositions were monitored every 3 min for at least 30 min to avoid transient responses. The steady-state gas compositions were measured at least 10 times (i.e. for at least another 30 min). The standard deviation of each data point was typically less than 5 %. The reaction rate was calculated from the amount of carbon dioxide produced and normalized by the weight of catalyst.

3. RESULTS AND DISCUSSION

Transmission electron microscopy (TEM) images of the pure ceria, 25 mol % MB Fe−Ce−O, 25 mol % MB Ni−Ce−O, and 25 mol % MB Cu−Ce−O particles are shown in Figure 1. In all cases, the absence of particles greater than 100 nm in diameter suggests that the precursor droplets are vaporized completely in the flame and that the particles form by gas-to-particle conversion following reaction of the precursor species to form metal oxides.

The selected area electron diffraction (SAED) pattern is indexed to polycrystalline CeO_2 in the fluorite structure. Similarly, parts b−d of Figure 1 show the bright field electron micrographs of the multicomponent oxide particles. From the micrographs, it is clear that the particle morphology is similar to that of the pure CeO_2 particles. The selected area electron diffraction patterns show polycrystalline CeO_2 in the fluorite structure, and no line corresponding to Cu, Ni, and Fe or any of the oxides of Cu, Ni, and Fe is detected. The surface area and particle diameter of pure CeO_2 and Cu−Ce−O, Ni−Ce−O, and Fe−Ce−O catalysts are given in Table 1. The primary particle diameters range from 3 to 10 nm, and the surface areas of the as-prepared catalysts are in the range of 127−163 m^2/g.

Thermogravimetric analysis (TGA) was performed in air at a heating rate of 283 K/min. The TGA curve of asprepared pure CeO_2, shown in Figure S1a in the Supporting Information, indicates that there were two stages of weight loss. The first weight loss of ∼1 % (between 293 and 473 K) was due to the removal of water, present in the sample because of water condensation. The sources of water are the precursor solution and the water formed as a combustion byproduct. The second stage of weight loss of ∼1 % (between 573 and 873 K) resulted from the oxidation of carbon compounds, likely from incompletely decomposed metal acetate precursors. Above 873 K, the weight is almost constant. Similarly, the TGA of the as-prepared 40 mol % MB Cu−Ce−O and 40 mol % MB Fe−Ce−O (in Figure S1b,c) showed the presence of ∼2 % of carbon compound. However, the amount of

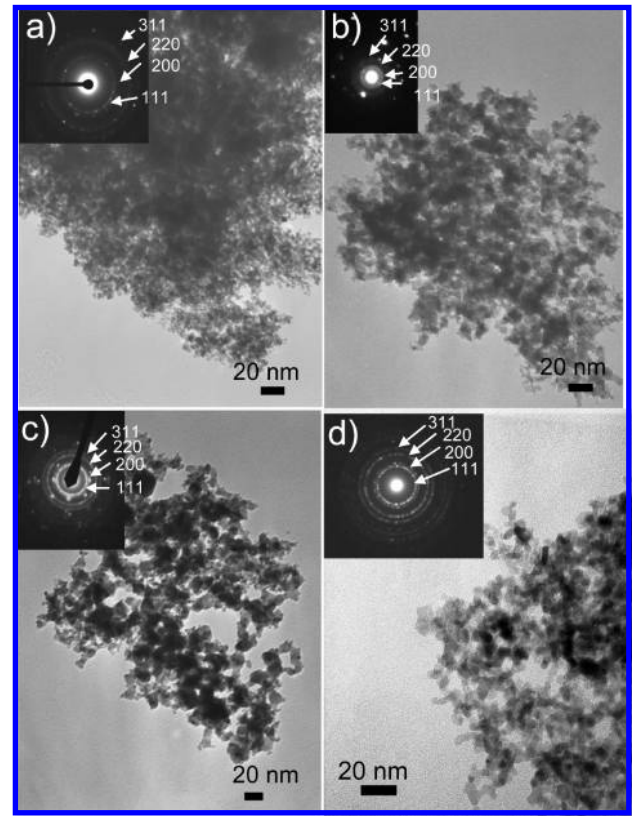

FIGURE 1. Transmission electron micrograph and selected area electron diffraction (SAED) patterns of (a) pure CeO_2, (b) 25 mol % MB Fe−Ce−O, (c) 25 mol % MB Ni−Ce−O, and (d) 25 mol % MB Cu−Ce−O catalysts.

Table 1. Comparative Study of the Particle Diameter and BET Surface Area of As-Prepared Pure CeO_2, Cu−Ce−O, Ni−Ce−O, and Fe−Ce−O Catalysts

materials system	av particle size[a] from TEM (nm)	std dev (nm)	BET surface area (m^2/g)	particle diameter from BET (nm)
CeO_2	4	2	154	5
10 mol % MB Cu−Ce−O	6	2	153	5
20 mol % MB Cu−Ce−O	7	2	153	5
25 mol % MB Cu−Ce−O	7	2	152	5
30 mol % MB Cu−Ce−O	6	3	153	5
40 mol % MB Cu−Ce−O	7	4	156	5
25 mol % MB Fe−Ce−O	8	4	122	6
40 mol % MB Fe−Ce−O	8	4	127	6
25 mol % MB Ni−Ce−O	7	2	160	5
40 mol % MB Ni−Ce−O	6	2	163	5

[a] A total of 150 particles were counted for each composition.

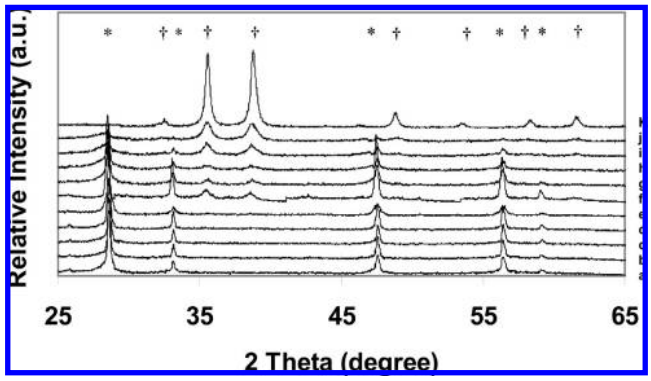

FIGURE 2. X-ray diffraction study of the as-prepared catalysts: (a) pure CeO_2; (b) 10 mol % MB Cu−Ce−O; (c) 20 mol % MB Cu−Ce−O; (d) 25 mol % MB Cu−Ce−O; (e) 40 mol % MB Cu−Ce−O; (f) 45 mol % MB Cu−Ce−O; (g) 50 mol % MB Cu−Ce−O; (h) 60 mol % MB Cu−Ce−O; (i) 80 mol % MB Cu−Ce−O; (j) 90 mol % MB Cu−Ce−O; (k) 100 mol % MB Cu−Ce−O. Asterisks denote peaks corresponding to CeO_2, while plus signs denote peaks corresponding to CuO.

water present was 6% and 5% for 40 mol % MB Cu−Ce−O and 40 mol % MB Fe−Ce−O, respectively. The larger amount of water detected in the Cu−Ce−O and Fe−Ce−O samples as compared to that in pure CeO_2 possibly comes from the atmosphere. Since the experiments were done on different days, the amount of water absorbed depends on the amount of moisture present in the atmosphere on that particular day.

X-ray diffraction patterns of Cu−Ce−O with Cu concentration 0−100 mol % MB are shown in Figure 2. The diffraction lines correspond to the fluorite-type structure, and the *d* values agree well with those expected for CeO_2. The diffraction lines of Cu-doped CeO_2 are broader than those of pure CeO_2, but peaks corresponding to Cu or CuO could not be detected, even with increasing Cu content up to 40 mol %. Two possible explanations are either that $Cu/Cu^{2+}/Cu^{+}$ species are only present on the CeO_2 surface, forming a monolayer/submonolayer, which does not alter the structure of the CeO_2 lattice and therefore $Cu/Cu^{2+}/Cu^{+}$ are not seen in the XRD pattern or that they substitute cerium in the ceria lattice, causing lattice distortion and leading to a shift or broadening of peaks in XRD. However, in the case of 45 mol % MB Cu−Ce−O (Figure 2f) the formation of the CuO phase is detected with CeO_2 as the major phase. This may be because either a small amount of CuO is formed as a separate phase in addition to the formation of a monolayer/submonolayer of CuO on the surface of CeO_2 or CuO is present as a multilayer and is crystalline on the surface of CeO_2. Diffraction patterns of 40 mol % MB Ni−Ce−O and 40 mol % MB Fe−Ce−O prepared by the flame synthesis method, shown in Figure S2 in the Supporting Information, are similar to those of pure CeO_2 and Cu-doped CeO_2 up to 40 mol %, in that NiO and Fe_2O_3 are not detected. The crystallite size calculated from Scherer's equation was ~3 nm, which is nearly same for 25 and 40 mol % MB Cu−Ce−O, Ni−Ce−O, and Fe−Ce−O materials.

The surface coverage of CuO on CeO_2 can be estimated in the following way. Assuming a 5 Å thickness of the CuO layer on CeO_2 particles with a total diameter of 5 nm, the core volume is 33 nm^3 and the volume of the CuO shell is

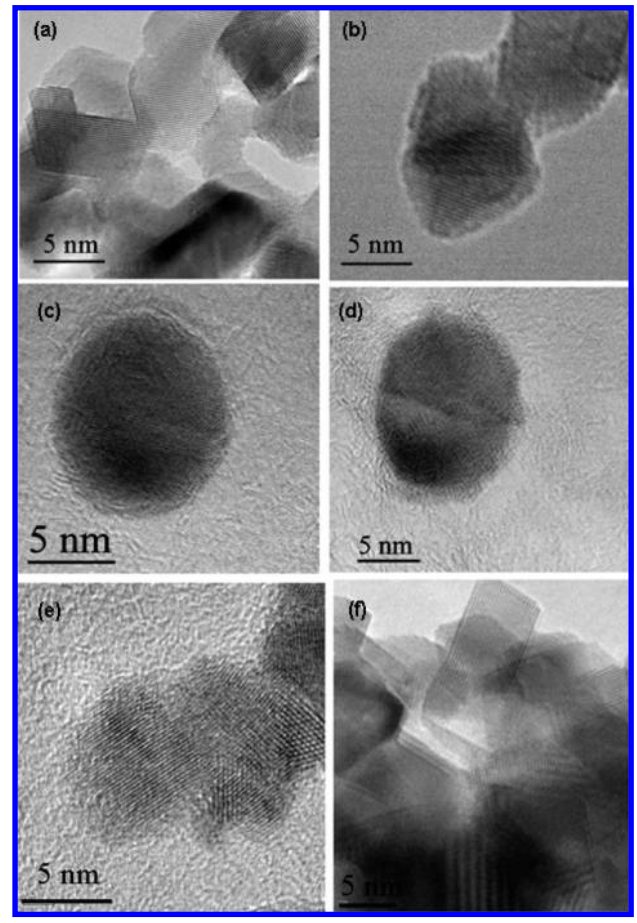

FIGURE 3. High-resolution transmission electron micrographs of (a) pure CeO_2, (b) 25 mol % MB Cu−Ce−O, (c) 25 mol % MB Ni−Ce−O, (d) 25 mol % MB Fe−Ce−O, and (e) 50 mol % MB Cu−Ce−O catalysts and (f) 25 mol % MB Cu−Ce−O after etching with nitric acid.

32 nm^3. Thus, the shell volume is ~50% of the total volume, which is equivalent to 23 mol % of CuO. Therefore, it may be possible that all CuO in 25 mol % MB Cu−Ce−O is at the surface in a monolayer. In the case of Cu−Ce−O particles with higher Cu loadings, this is likely multilayer coverage with the degree of CuO crystallinity increasing with increasing Cu content. As the CuO concentration increases beyond 45 mol %, the CuO diffraction peak intensity increases and finally the pure CuO phase was detected for 100 mol % MB Cu−Ce−O, as shown in Figure 2k.

To further investigate the particle morphology, a high-resolution transmission electron microscopic study was performed. HRTEM images of pure ceria, 25 mol % MB Cu−Ce−O, 25 mol % MB Ni−Ce−O, 25 mol % MB Fe−Ce−O, 50 mol % MB Cu−Ce−O, and 25 mol % MB Cu−Ce−O after etching with nitric acid are shown in Figure 3. Figure 3a shows pure ceria with particles faceted in shape. For the ceria nanoparticles doped with 25 mol % Cu, the particles are more rounded in shape and their surface is covered with an amorphous layer (Figure 3b). Similarly, in the case of ceria nanoparticles doped with 50 mol % Cu, the surface is covered, presumably by amorphous CuO (Figure 3e). However, an X-ray diffraction study of a 50 mol % Cu−Ce−O sample indicates the presence of both crystalline CuO and

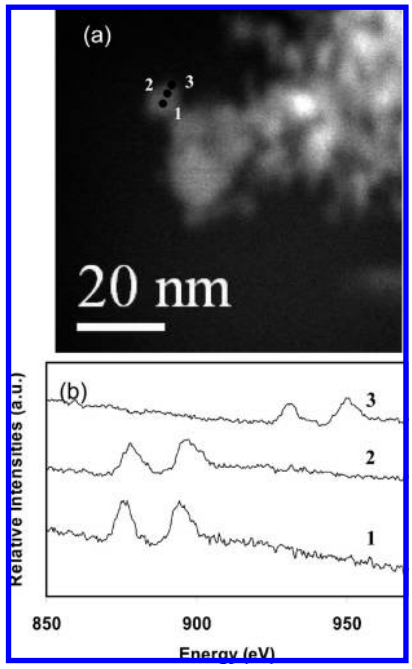

FIGURE 4. (a) Dark field STEM image of a 25 mol % MB Cu−Ce−O particle and (b) normalized EELS spectra (Ce M edge and Cu L edge) of a 25 mol % MB Cu−Ce−O particle at three different points.

CeO_2. Therefore, a mixture of amorphous and crystalline CuO is present in the 50 mol % Cu−Ce−O sample. The amorphous CuO is not present on the surface of faceted CeO_2 particles after etching the 25 mol % MB Cu−Ce−O sample with nitric acid, which is shown in Figure 3f. This indicates the possible formation of core−shell structured Cu−Ce−O material, likely with CeO_2 in the core and CuO in the shell or separate CeO_2 and CuO particles. Similarly, in the case of ceria nanoparticles doped with 25 mol % MB Ni−Ce−O and Fe−Ce−O, thin amorphous layers of presumably NiO and Fe_2O_3, respectively, are detected, which are shown in Figure 3c,d.

Electron energy loss spectroscopy (EELS) was used to better understand the nature of the synthesized Cu−Ce−O, Ni−Ce−O, and Fe−Ce−O materials. Figure 4a shows the DF-STEM image of a nearly isolated Cu−Ce−O particle. Subnanometer EELS measurements were carried out on the spherical nanoparticles at the edge of an agglomerate for each of the Cu−Ce−O, Ni−Ce−O, and Fe−Ce−O materials. The EELS spectra were collected from three different probe locations on one particle; at the center (point 1), between the center and the edge (point 2), and at the edge (point 3), indicated in Figure 4a (Cu−Ce−O particle). Figure 4b shows the EELS spectra of the Cu−Ce−O particle at these three points. From Figure 4b it is clear that both Cu (L_2 and L_3 edges at 931 and 951 eV) and Ce (M_4 and M_5 edges at 883 and 901 eV) are present both at points 1 and 2. However, only Cu was found with no Ce signal at point 3. Similar results were found in the case of Ni−Ce−O and Fe−Ce−O particles, which are shown in Figures 5 and 6 respectively. These results clearly suggest the formation of Cu−Ce−O, Fe−Ce−O, and Ni−Ce−O particles with core−shell structures.

Figure 7 depicts the Fourier transform (FT) magnitudes of k^2-weighted EXAFS for Ce, Cu, Fe, and Ni in the 25 mol

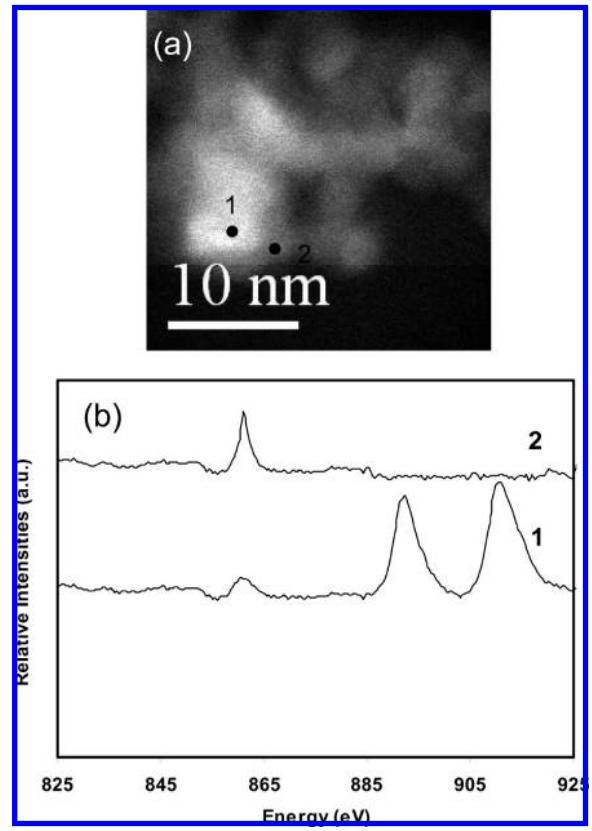

FIGURE 5. (a) Dark field STEM image of a 25 mol % MB Ni−Ce−O particle and (b) normalized EELS spectra (Ce M edge and Ni L edge) of a 25 mol % MB Ni−Ce−O particle at two different points.

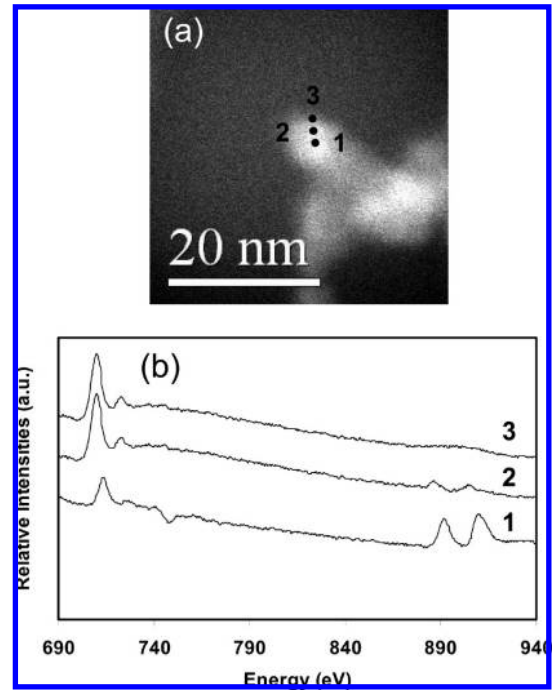

FIGURE 6. (a) Dark field STEM image of a 25 mol % MB Fe−Ce−O particle and (b) normalized EELS spectra (Ce M edge and Fe L edge) of a 25 mol % MB Fe−Ce−O particle at three different points.

% MB M−Ce−O systems as well as the corresponding bulk oxides. As expected for a host material with dilute dopant concentration, the FT magnitudes of Ce L_3 edge data in 25 mol % MB M−Ce−O and reference CeO_2 samples agree

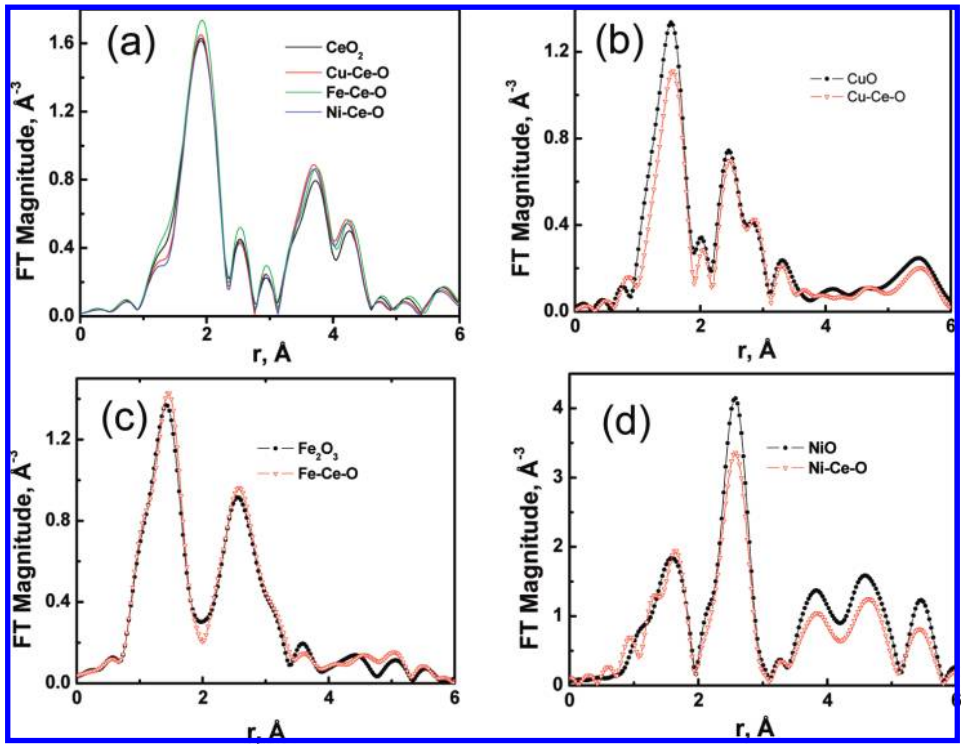

FIGURE 7. Fourier transform of k^2-weighted EXAFS spectra: (a) Ce L_3-edge data of CeO_2, 25 mol % MB Cu−Ce−O, 25 mol % MB Fe−Ce−O, and 25 mol % MB Ni−Ce−O; (b) Cu K-edge data for Cu−Ce−O compared to CuO; (c) Fe K-edge data for Fe−Ce−O compared to Fe_2O_3; (d) Ni K-edge data for Ni−Ce−O compared to NiO.

within experimental uncertainties (Figure 7a). From the analysis of the K-edge EXAFS spectra of the dopants, it can be concluded that the dopants in all 25 mol % MB M−Ce−O systems are isostructural with their oxide counterparts, as shown in Figure 7b−d. This evidence corroborates the conclusion from other techniques that the dopant materials form separate oxide phases (CuO, Fe_2O_3, NiO) within the host matrix (CeO_2), with the possible exception of Fe, where this effect is least pronounced. The slightly lower amplitude of FT magnitudes of the first two peaks (corresponding to the M−O and M−M bonds) relative to their counterpart oxides was observed in all 25 mol % MB Cu−Ce−O and Ni−Ce−O systems, reflecting more disordered and/or smaller particle size of the nanophase mixed oxides, which was independently verified by theoretical analysis of EXAFS data.

X-ray photoelectron spectra were collected for four samples: pure CeO_2, 25 mol % MB Fe−Ce−O, 25 mol % MB Cu−Ce−O, and 25 mol % MB Ni−Ce−O. Ce 3d, Fe 2p, Cu 2p, and Ni 2p core-level spectra are shown in Figure 8 along with Ce/transition metal ratios collected from argon-ion sputter profile studies. Ce was found to be in the +4 oxidation state for all four samples, as evidenced in Figure 8A by the characteristic six-peak structure corresponding to three pairs of spin−orbit doublets due to different Ce 4f level occupancies in the final state; these spectra are also consistent with those reported previously for CeO_2 (44, 45). As CeO_2 has been shown to undergo photoreduction during XPS collection, the Ce 3d peaks were collected within only 20 min of exposure to X-rays; there is no evidence of peaks due to Ce^{3+}. Carbon was detected on the surface of all samples as mainly adventitious hydrocarbon, with some C−O functionality, possibly from surface hydroxyls, and carbonate species. As mentioned earlier, TGA studies show the presence of ~1 wt % of carbon in pure CeO_2 and ~2 wt % of carbon in both Cu−Ce−O and Fe−Ce−O samples. The XPS results for the C 1s region reveal that ~0.2−0.5 wt % of this carbon is due to the carbonate species present in all the samples.

For the Cu−Ce−O sample the Cu $2p^{3/2}$ and Cu $2p^{1/2}$ peaks fall at 933.6 and 953.2 eV respectively, with shake-up satellites, unique to the +2 oxidation state, appearing at 941.1 and 962.2 eV, consistent with those found previously for CuO (46). The Fe 2p region for the Fe−Ce−O sample, part IIIB of Figure 8 shows that Fe has four peaks, Fe $2p^{3/2}$ at 711.4 eV, Fe $2p^{1/2}$ at 724.8 eV, and satellite peaks, unique to the +3 oxidation state, at 718.5 and 732.6 eV, which is consistent with Fe_2O_3 (47). Part IVB of Figure 8 shows Ni $2p^{3/2}$ for the Ni−Ce−O sample, having a main peak at 854.7 eV and a satellite peak at 860.5 eV, consistent with NiO (48); only one oxidation state, +2, is known to exist for nickel oxide.

Several pieces of evidence within the XPS spectra support the formation of a core−shell type structure. First, the atomic concentrations calculated suggest much higher concentrations, 40% for Cu, 62% for Fe, and 39% for Ni of metal ions compared to cerium, than the experimental bulk values of 25 mol %. The percent atomic concentrations are calculated with the assumption that the sample is homogeneous throughout the depth to which XPS can probe (~10 nm). If the samples were homogeneous, we would expect the atomic percentage calculated by this method to be 25%; the increased percentages indicate significant surface seg-

regation whereby the signal from the overlying copper, nickel, or iron is attenuating the signal from the underlying cerium. The highest concentration (62%) observed for Fe in the Fe−Ce−O sample can be explained by the fact that Fe_2O_3 has the lowest density (5.52 g/cm^3) compared to CuO (6.31 g/cm^3) and NiO (6.7 g/cm^3); the higher density of the Fe_2O_3 leads to a thicker film thus greater attenuation of the underlying cerium when compared to the copper and nickel.

Further evidence for the core−shell structure can be found by comparing the photoelectric peak area to the increase in background ratio in the Ce 3d region. The photoemission process can be both elastic and inelastic, with elastic electrons giving rise to photoelectric peaks with discrete binding energies and inelastic electrons, usually suffering energy loss due to collisions on escape through the surface, contributing to the background. For systems with inhomogeneous concentration profiles, there will be a change in the ratio of inelastic scattering to elastically escaped electrons, when compared to a homogeneous sample. This phenomenon has been extensively studied by Tougaard, and we use a modified version of his previously described method (49) that can be applied to the Ce 3d region. The ratios were calculated using the equation

$$D = \frac{I_{Ce\ 3d}}{B} \quad (2)$$

where $I_{Ce\ 3d}$ is the Ce 3d peak area and B is the increase in background measured at 40 eV to higher binding energy of the peak labeled with an asterisk, as detailed in Figure 8A. The linear background was taken from a binding energy of 5 eV lower and 40 eV higher than the peak labeled with an asterisk. For CeO_2, $D = 8.5$ eV, and for Fe−Ce−O, Cu−Ce−O, and Ni−Ce−O, $D = 6.7$, 6.5, 6.2 eV, respectively. The lower value of the ratios for the mixed metal oxide samples indicate a greater amount of inelastic scattering of the Ce 3d electrons as compared to the CeO_2 sample, meaning that the Ce 3d electrons are escaping from deeper within the surface in comparison to the CeO_2 sample.

Argon ion depth profiling in combination with XPS was used to further study concentration as a function of depth; the results are shown in Figure 8C, plotted as the ratio of % M to % Ce atomic concentration versus sputter time. In all cases, the results show a much higher ratio of metal to cerium initially, with the concentration of metal decreasing with time. In the case of Fe and Ni the concentration

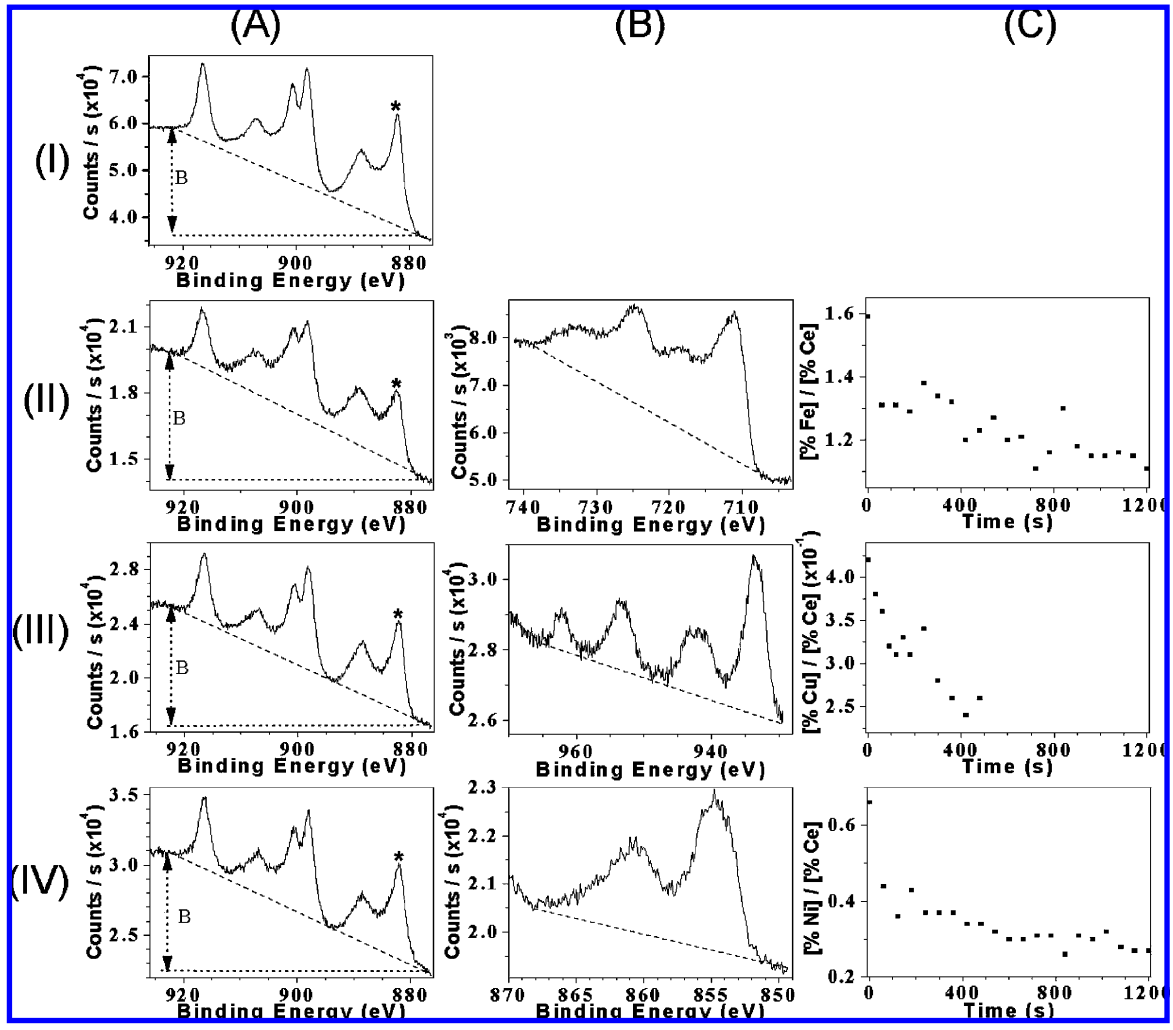

FIGURE 8. Core-level X-ray photoelectron spectra of (A) Ce 3d, (B) M 2p (M = Fe, Cu, Ni) and (C) M:Ce atomic percentage composition ratios calculated from argon ion sputter profile data: (I) CeO_2: (II−IV) 25% MB M−Ce−O, where M = Fe, Cu, Ni, respectively.

Table 2. Elemental Composition of Cu−Ce−O Catalysts Obtained from Atomic Absorption Spectra (Standard Deviation ±5%)

	Cu/Ni/Fe (mol %)		
sample	precursor material	final product before etching	final product after etching
10 mol % MB Cu−Ce−O	10	12	<0.01
20 mol % MB Cu−Ce−O	20	21	<0.01
25 mol % MB Cu−Ce−O	25	27	1.40
40 mol % MB Cu−Ce−O	40	39	0.50
50 mol % MB Cu−Ce−O	50	51	0.20
25 mol % MB Ni−Ce−O	25	27	0.15
25 mol % MB Fe−Ce−O	25	28	7.25

becomes more or less constant after ~500 s; unfortunately the data for the copper sample were only collected for 480 s of sputtering. Assuming there is no significant preferential sputtering, these results are consistent with a core−shell structure where the first 500 s involves sputtering away some of the outer shell of the structure, revealing the inner cerium core, resulting in a gradually lower signal from the Cu metal shell and a higher signal from the cerium core. Eventually, due to size distribution of the nanoparticles and the uneven surface of the powder studied, the concentrations would be expected to even out, as is seen in the case of the nickel and iron samples.

The surface CuO, NiO, and Fe_2O_3 in the Cu−Ce−O, Ni−Ce−O, and Fe−Ce−O systems could be removed by etching the sample with nitric acid. Table 2 gives a comparison of the amount of Cu, Ni, and Fe present in mol % MB in the starting solution, in the flame-synthesized Cu−Ce−O, Ni−Ce−O, and Fe−Ce−O samples, and in the etched Cu−Ce−O, Ni−Ce−O, and Fe−Ce−O samples. The results indicate that the amounts of Cu in 10, 20, 25, 40, 50, and 60 mol % MB Cu−Ce−O, Ni in 25 mol % MB Ni−Ce−O, and Fe in 25 mol % MB Fe−Ce−O samples are similar in the starting materials versus flame-synthesized Cu−Ce−O, Ni−Ce−O, and Fe−Ce−O samples, respectively. However, after etching, the amounts of Cu and Ni present are much smaller compared to those in the as-prepared flame-synthesized samples. This suggests that most of the Cu and Ni on the CeO_2 surface is present as bulk CuO and NiO, which is dissolved by nitric acid. Either the small portion of Cu and Ni which remained is likely present as oxide clusters in CeO_2 (12) or Cu^{2+} and Ni^{2+} are incorporated in the CeO_2 lattice, considering the atomic radii of Cu, Ni, and Ce as 1.57, 1.49, and 2.70 Å, respectively (45). Similarly, in the case of the 25 mol % Fe−Ce−O sample, the amount of Fe present in the etched sample is also much smaller compared to the Fe present in the as-prepared sample but higher compared to Cu−Ce−O and Ni−Ce−O samples. This is probably because Ce is substituted by Fe or Fe present in CeO_2 in the form of clusters, which is supported by EXAFS results, indicating a more disordered structure as compared to Cu−Ce−O and Ni−Ce−O samples.

This apparent formation of a core−shell structure can be better understood by considering likely particle formation and growth mechanisms. In the flame, the reaction of the precursors to form oxide species is fast and thus both CeO_2 and transition-metal oxide species are formed simultaneously. Because of the low vapor pressures of these species (50) and resulting high saturation ratios, the critical droplet diameter is very small and, thus, the nucleation is expected to be kinetic and growth is limited only by the rate of collisions between clusters (51).

In the case of single-component oxides, it is expected that pure CeO_2 nanoparticles formed initially are solid-like, considering the high melting point of CeO_2 (2673 K) and our maximum flame temperature of 1773 K. However, pure CuO and Fe_2O_3 nanoparticles may be liquid as formed, as their melting temperatures, 1608 K and 1823 K, respectively, are almost equal to or less than the flame temperature. NiO may be solid because of its higher melting temperature of 2233 K; however, because of the nanocrystalline nature the melting temperature of NiO may decrease, resulting in liquid particles, which is supported by the estimated decrease in melting temperature of Cr_2O_3 nanoparticles by Guo et al. (52).

In the case of mixed oxides, particle formation and the evolution of the arrangement of species is likely more complicated. In the experimental and molecular dynamics studies of titania-doped CeO_2 by Feng et al., it was shown that CeO_2 in the nanoparticles generated in the flame (flame temperature at about 2773 K) was likely crystalline, while the TiO_2 was likely in a molten state (the melting temperature of TiO_2 is 2116 K). CeO_2 occupied the core region of the nanoparticle and was covered by an amorphous TiO_2 shell with a limited portion of Ti^{4+} incorporated into the CeO_2 lattice. Molecular dynamics simulations indicated that TiO_2 does not crystallize as the crystallization front moves from the CeO_2 core out to the surface. This was shown by Feng et al. to be driven by the system minimizing its surface energy, to form a thermodynamically more stable nanoparticle (42). Therefore, drawing an analogy between the behaviors of our materials to the phenomenon observed by Feng et al. for titania-doped CeO_2, it may be possible that in Cu−Ce−O, Ni−Ce−O, and Fe−Ce−O systems crystalline CeO_2 occupies the core region of the nanoparticles and is covered by a CuO, NiO, or Fe_2O_3 shell.

Recent density functional theory calculations by Shapovalov et al. for the CeO_2 (111) surface doped with Cu, Ag, and Au show that the bond between oxygen atoms and Ce is weakened in the presence of dopants (53). The dopant−oxygen distances in doped CeO_2 are greater than in the dopant's own oxide, and the distances between Ce and O atoms are shorter in Cu-doped ceria than in CeO_2 itself. It is also found by Shapovalov et al. that a dopant with lower valency than the cation it replaces creates an electron deficiency in its neighborhood. This weakens the bond between the oxide and the oxygen atoms in the neighborhood of the dopant. Additionally, a dopant changes the oxygen−oxide (host and dopant) bond distances if its own oxide has a crystal structure different from that of the host oxide. Therefore, it is difficult to maintain the number of oxygen atoms in this system to form a compound. In the present

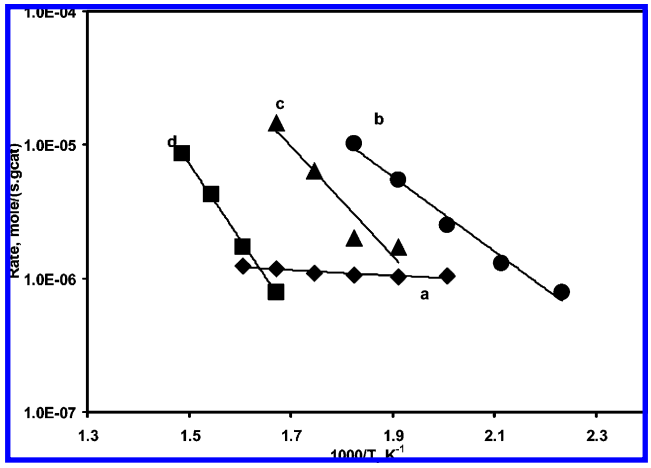

FIGURE 9. Water-gas shift activities of various flame-made ceria-based catalysts: (a) pure CeO_2; (b) 40 mol % MB Cu−Ce−O; (c) 40 mol % MB Ni−Ce−O; (d) 40 mol % MB Fe−Ce−O. All measurements were taken with 5 wt % H_2, 5 wt % CO, and a H_2O/CO ratio of 5.

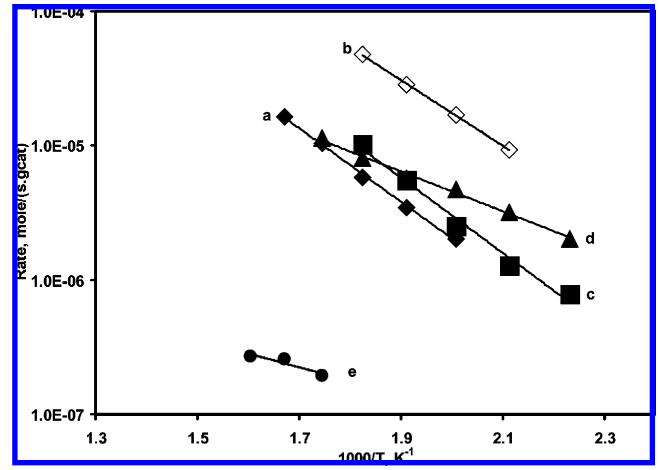

FIGURE 10. Water-gas activities of various Cu−ceria catalysts: (a) 15 mol % MB Cu−Ce−O with H_2/CO = 1; (b) 15 mol % MB Cu−Ce−O with H_2/CO = 0 or 5% CO with no H_2; (c) 40 mol % MB Cu−Ce−O with H_2/CO = 1; (d) 700 °C annealed 40 mol % MB Cu−Ce−O with H_2/CO ratio 1; (e) 1100 °C annealed 40 mol % MB Cu−Ce−O with H_2/CO = 1. All measurements were taken with H_2O/CO = 5.

study, the valencies of the dopants (Cu, Ni, and Fe) are less than that of Ce and so it is possible that the dopant oxides make physical mixtures rather than making a compound, which is also, supported by the AAS, EXAFS, and XPS results.

A comparison of the WGS activities on pure CeO_2, 40 mol % MB Cu−Ce−O, 40 mol % MB Ni−Ce−O, and 40 mol % MB Fe−Ce−O is shown in Figure 9. The feed gas contained 5 wt % CO, 5 wt % H_2, 25 wt % H_2O, and 65 wt % Ar. Fuel processors break down the hydrocarbon fuel into reformate, which contains smaller molecules, including H_2, CO, and others. Here, we investigated the catalytic properties at H_2/CO = 1, which is realistic for catalytic partial oxidation of diesel fuel (54). The pressure drops were less than 0.7×10^5 Pa and the conversions were less than 10 % for all reported results, and so differential conditions are assumed. Below 573 K ($1/T = 1.75 \times 10^{-3}$ K^{-1}), Cu−Ce−O has the highest shift activities at a given temperature, while Ni−Ce−O is more active than Fe−Ce−O. Figure 9 also shows that the pure CeO_2 can have a higher catalytic activity than Fe−Ce−O at low temperatures ($1/T = 1.67 \times 10^{-3}$ or $T = 598$ K). This suggests that the presence of surface Fe reduces the amount of CeO_2 active sites but the temperature is too low to activate the reactants on the Fe active sites. However, extrapolation of WGS reactivity of pure CeO_2 to temperatures lower than $T = 498$ K ($1/T = 2.01 \times 10^{-3}$ K^{-1}) is not appropriate, since we cannot detect activity below $T = 498$ K. No methane formation is observed in any case.

From Figure 9, the activation energies for Cu−Ce−O, Ni−Ce−O, and Fe−Ce−O were determined to be 53.6, 78.0, and 108.5 kJ/mol, respectively. Under CO-rich conditions and with the absence of H_2 in the reactant stream, Li et al. (55) found that the activation energies over Ce(La)O_x, Cu−Ce(La)O_x, and Ni−Ce(La)O_x were 30.4 and 38.2 kJ/mol, respectively. Both studies showed that the presence of Cu or Ni enhanced the WGS activity on ceria materials. Moreover, the presence of Cu on ceria materials provided a lower activation energy for WGS reaction than the presence of Ni. In contrast, the results showed that the presence of H_2 has an inhibitory effect on the WGS reaction on metal ceria, although the catalyst materials and reaction conditions (H_2O/CO and H_2/CO ratios) are not exactly the same. The difference of 23 and 40 kJ/mol in apparent activation energies over Cu−ceria and Ni−ceria indicates that the presence of H_2 increases the apparent activation energy, which is consistent with the inhibitory effects of H_2 on WGS reactions.

As mentioned earlier, Figure 9 shows that pure ceria can have a higher catalytic activity than Fe−Ce−O at low temperatures ($1/T = 1.67 \times 10^{-3}$ K^{-1} or $T = 598$ K). According to the redox mechanism of WGS on metal−ceria catalysts (55), CO molecules adsorbed on the metal clusters react with oxygen transported to the metal−ceria interface from ceria. Water dissociates on an oxygen vacancy site on ceria to H_2 and atomic oxygen. This water dissociation reaction reoxidizes the ceria. Our results suggest that the presence of surface Fe may reduce the amount of ceria active sites, while the temperature (598 K) is too low to activate the reactants on the Fe active sites. This is consistent with a synergistic WGS reaction described by the redox mechanism.

Figure 10 illustrates the WGS activities of the Cu−Ce−O catalyst under various conditions. One may argue that the presence of H_2 activates Cu−Ce−O by reduction of copper oxides into metallic copper, which is commonly accepted as the active copper phase for WGS catalysts, including commercial CuO−ZnO−Al_2O_3 catalyst (56, 57). Similarly, in the case of Ni−MoO_2, the active species detected was Ni, which was generated during the water-gas shift reaction (58). In the present study, XPS analyses of the as-prepared nanoparticles show that the transition metals were present in the catalysts as Cu^{2+}, Ni^{2+}, and Fe^{3+}, and the amount of Cu^0, Ni^0, and Fe^0 or Cu^+, Ni^{2+}, and Fe^{2+} was negligible. However, XPS studies (Figures S3 and S4 in the Supporting Information) of the WGS treated for 40 mol % MB Cu−Ce−O and 40 mol % MB Ni−Ce−O samples after reaction indicate that the oxidation states of Cu and Ni were 0. This suggests the reduction of CuO and NiO to Cu and Ni, respectively, by CO and/or H_2 during the WGS reaction. Similar results, not shown, were obtained for Fe−Ce−O. This suggests that the

major active species for the WGS reaction were metallic Cu, Ni, and Fe in the Cu−Ce−O, Ni−Ce−O, and Fe−Ce−O systems, respectively. Figure 10 also shows that the 40 mol % MB Cu−Ce−O gives higher activities compared to 15 mol % MB Cu−Ce−O (Figure 10a,c), indicating the WGS activities depend on Cu loading (59).

In addition, annealing of the 40 mol % MB Cu−Ce−O sample at 973 K results in better activity in comparison to the as-prepared catalyst at temperatures below 523 K, because annealing the catalyst at 973 K increases the apparent activation energy of the WGS reaction at temperatures below 523 K. However, annealing at 1373 K reduces the activity dramatically because the heat treatment decreases the surface area of the catalyst and possibly increases the particle size, explaining the change of activation energy upon annealing. This difference can be explained by FTIR studis of the as-prepared and annealed samples. The FTIR spectrum (Figure S5 in the Supporting Information) of the as-prepared 40 mol % MB Cu−Ce−O shows vibration modes at 1354 and 1519 cm^{-1}. These peaks correspond to the O−C−O symmetric and asymmetric stretching modes. In addition, there is no C−H stretching mode around 2900 cm^{-1}. Therefore, the 1354 and 1519 cm^{-1} modes are likely to be the carbonate peaks. These assignments are consistent with a study on thermal decompositions of cerium(III) acetate. Arii et al. proposed that the cerium(III) acetate decomposed to CeO_2 via $Ce_2O(CH_3CO_2)_4$, $Ce_2O_2(CH_3CO_2)_2$, and $Ce_2O_2CO_3$ as the decomposition intermediate products (60). The possible origin of the surface carbonate in the present study is the residue of the metal acetate precursors during flame combustion synthesis. Therefore, on comparison of the intensity of the carbonate bands, the FTIR spectra (Figure S5) suggests that the as-prepared sample has many more surface carbonate species as compared to the sample annealed at 973 K. The indicates that the formation of carbonate species is one of the reasons for deactivation of various flame-synthesized as-prepared WGS catalysts, which is consistent with some other studies in the literature (13, 61). However, above 523 K, the WGS activity dropped, which may be due to a loss of surface area (42 m^2/g, annealed at 973 K, a loss of surface area by 63%) and an increase in particle size of the catalyst. This is supported by Li et al., who suggested that the loss of surface area and the formation of bulk CuO particles, which have negligible interaction with CeO_2, contribute to the activity loss (55).

The WGS activities of Cu−Ce−O with various Cu contents are shown in Figure 11. It is clear from the figure that there is an increase in WGS activity from 15 mol % MB to 25 mol % MB Cu loading but the activity drops as the Cu loading increases from 25 mol % to 40 mol %. O'Brien et al. have demonstrated that the WGS activity increases with increase in the Cu loading (62). Also, Bukur et al. have reported that copper loading increases the WGS activity (63). However, Li et al. have shown that there is no appreciable difference in the WGS light-off temperature over Cu−Ce(La)O_x catalysts with different copper loadings from 5 to 40 at % (55). In our case, the apparent maximum in activity at 25 mol % may

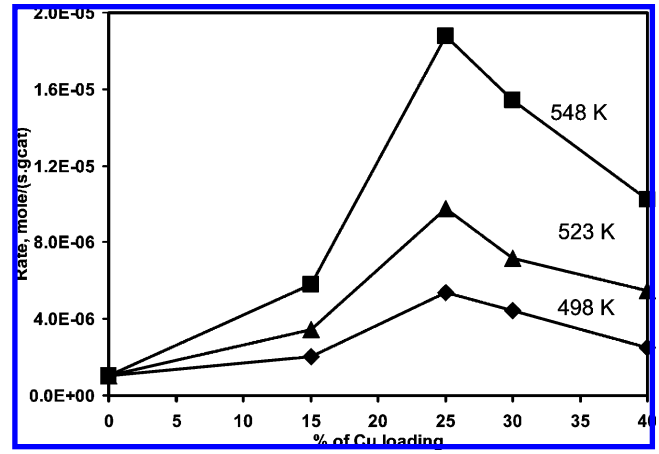

FIGURE 11. Water-gas shift activities of Cu−Ce−O catalysts at different temperatures as a function of Cu loading.

be due to slight differences in the morphology of Cu^{2+} clusters as the composition changes. In a related study, Rodriguez et al. showed that the water-gas shift activity of Cu−CeO_2 changes with the morphology of the catalyst particle (64). They found that the WGS activity increased with an increase in the amount of Cu monolayer on the CeO_2 surface and reached a maximum at 0.5 monolayer, where the particle size increased from 2−4 nm to above 4 nm. The activity decreased as the amount of monolayer increased, resulting in an increase in particle size. In case of 25 mol % MB Cu−Ce−O, the amount of Cu^{2+} that could not be removed by etching is 1.4 mol %, while this amount is 0.5 mol % in case of 40 mol % MB Cu−Ce−O (Table 2). Another explanation is that, at 25 mol % MB Cu, there may be near-monolayer CuO coverage on the surface of CeO_2, which after reduction provides maximum active sites for CO interactions, while still facilitating oxygen exchange with ceria. At higher copper loadings, and presumably thicker coatings, these important support interactions may be reduced.

4. CONCLUSIONS

Flame synthesis is an easy, single-step method for the preparation of pure CeO_2 and transition-metal-doped CeO_2 materials starting from aqueous solutions of metal salts. The particle diameters of the synthesized materials are in the range of 3−10 nm, and the BET surface areas are in the range of 127−163 m^2/g. In the Cu−Ce−O, Ni−Ce−O, and Fe−Ce−O systems, the CeO_2 is believed to be likely in the core with CuO, NiO, or Fe_2O_3 present on the surface of the particles as a shell, as indicated by the presence of an amorphous layer on the surface of crystalline ceria, observed by HRTEM. This model is consistent with the EXAFS and XPS analysis results and etching studies. EXAFS results indicate the doping materials form separate oxide phases (CuO, Fe_2O_3, NiO), and surface enrichment of the transition metals on the CeO_2 crystals was detected using XPS. Further confirming surface enrichment, etching studies revealed that most of the oxides could be removed by nitric acid, with only a small amount of Cu and Ni (<2 mol %) and Fe (~7 mol %) remaining in the particles, likely dissolved in the CeO_2 lattice. The core−shell nature of the particles is confirmed by

electron energy loss spectroscopy (EELS). From XPS, it is clear that the transition metals (Cu, Ni, and Fe) in the as-prepared samples are in an oxidized state but they are reduced to the metallic state under WGS conditions. The WGS activity results for flame-synthesized metal ceria catalysts show that the Cu−Ce−O catalyst has higher activity compared to Ni−Ce−O and Fe−Ce−O catalysts. The active species for the WGS reaction were metallic Cu, Ni, and Fe. Notably, no methane formation was observed for these catalysts over the range of our experimental conditions. Heat treatment increases the activation energy of the WGS reaction at low temperature, reduces the surface area, and increases the particle diameter. Calcination of the sample removes the surface carbonates and water species, confirmed by FTIR. These combined effects contribute a higher activity at lower temperature but a lower activity at higher temperature when compared with the as-prepared catalyst. It is determined that the optimum bulk copper loading for the flame-synthesized Cu−Ce−O catalyst is 25 mol %.

Acknowledgment. We thank Amy Wingfield, Jason Repac, and Radhika Char for help in synthesizing the particles. Support from the National Science Foundation under Grant No. DMR-0080008 for the purchase of the X-ray photoelectron spectrometer is acknowledged. This work was partially supported by the US Army Research Laboratory, Contract No. W911QX-04-C-0105. R.K.P. and S.H.E. thank the U.S. Army Research Laboratory for instrument usage. A.I.F. and Q.W. gratefully acknowledge the support of this work by the Department of Energy, Basic Energy Sciences, under Grant No. DE-FG02-03ER15476. Use of the NSLS was supported by the U.S. Department of Energy, Office of Science, Office of Basic Energy Sciences, under Contract No. DE-AC02-98CH10886. Beamline X18B at the NSLS is supported in part by the Synchrotron Catalysis Consortium, U.S. Department of Energy Grant No. DE-FG02-05ER15688. Support of the Maryland NanoCenter and its NispLab is also acknowledged. The NispLab is supported in part by the National Science Foundation as an MRSEC Shared Experimental Facility.

Supporting Information Available: Figures giving thermogravimetric analysis (TGA) data, X-ray photoelectron spectra (XPS), X-ray diffraction (XRD) patterns, and Fourier transform infrared (FTIR) spectra of flame-made catalysts. This material is available free of charge via the Internet at http://pubs.acs.org.

REFERENCES AND NOTES

(1) Wyckoff, R. W. W. *Crystal Structures*, 2nd ed.; Wiley-Interscience: New York, 1963.
(2) Steele, B. C. H. *Solid State Ionics* **2000**, *129*, 95–110.
(3) Xia, B.; Lenggoro, I. W.; Okuyama, K. *J. Mater. Chem.* **2001**, *11*, 2925–2927.
(4) Wang, S.; Kato, T.; Nagata, S.; Kaneko, T.; Iwashita, N.; Honda, T.; Dokiya, M. *Solid State Ionics* **2002**, *152*, 477–484.
(5) Rao, G. R.; Fornasiero, P.; DiMonte, R.; Kaspar, J.; Vlaic, G.; Balducci, G.; Meriani, S.; Gubitosa, G.; Cremona, A.; Graziani, M. *J. Catal.* **1996**, *162*, 1–9.
(6) Kaspar, J.; Fornasiero, P.; Graziani, M. *Catal. Today* **1999**, *50*, 285–298.
(7) Hirano, M.; Watanabe, S.; Kato, E.; Mizutani, Y.; Kawai, M.; Nakamura, Y. *Solid State Ionics* **1998**, *111*, 161–169.
(8) Trovarelli, A. *Catal. Rev.-Sci. Eng.* **1996**, *38*, 439–520.
(9) Kusar, H.; Hocevar, S.; Levec, J. *Appl. Catal. B: Environ.* **2006**, *63*, 194–200.
(10) Liu, C. T.; Shi, P. F.; Zhang, J. X. *J. Rare Earths* **2004**, *22*, 864–866.
(11) Tschöpe, A.; Liu, W.; Flytzani-Stephanopoulos, M.; Ying, J. Y. *J. Catal.* **1995**, *157*, 42–50.
(12) Qi, X. M.; Flytzani-Stephanopoulos, M. *Ind. Eng. Chem. Res.* **2004**, *43*, 3055–3062.
(13) Hilaire, S.; Wang, X.; Luo, T.; Gorte, R. J.; Wagner, J. *Appl. Catal. A: Gen.* **2001**, *215*, 271–278.
(14) Wang, X.; Gorte, R. J.; Wagner, J. P. *J. Catal.* **2002**, *212*, 225–230.
(15) Fu, Q.; Saltsburg, H.; Flytzani-Stephanopoulos, M. *Science* **2003**, *301*, 935–938.
(16) Rodriguez, J. A.; Liu, R.; Hrbek, J.; Perez, M.; Evans, J. *J. Mol. Catal. A: Chem.* **2008**, *281*, 59–65.
(17) Su, Y.; Wang, S. P.; Zhang, T. Y.; Wang, S. R.; Zhu, B. L.; Cao, J. L.; Yuan, Z. Y.; Zhang, S. M.; Huang, W. P.; Wu, S. H. *Catal. Lett.* **2008**, *124*, 405–412.
(18) Luo, J. Y.; Meng, M.; Yao, J. S.; Li, X. G.; Zha, Y. Q.; Wang, X.; Zhang, T. Y. *Appl. Catal. B: Environ.* **2009**, *87*, 92–103.
(19) Pradhan, S.; Reddy, A. S.; Devi, R. N.; Chilukuri, S. *Catal. Today* **2009**, *141*, 72–76.
(20) Sahoo, S. K.; Mohapatra, M.; Pandey, B.; Verma, H. C.; Das, R. P.; Anand, S. *Mater. Charact.* **2009**, *60*, 425–431.
(21) Yang, X. C.; Lu, Z. G.; Kang, X. C.; Wei, Y. N. *J. Inorg. Mater.* **2009**, *24*, 187–191.
(22) Zhou, Y. C.; Rahaman, M. N. *J. Mater. Res.* **1993**, *8*, 1680–1686.
(23) Masui, T.; Fujiwara, K.; Machida, K.; Adachi, G.; Sakata, T.; Mori, H. *Chem. Mater.* **1997**, *9*, 2197–2204.
(24) Bumajdad, A.; Zaki, M. I.; Eastoe, J.; Pasupulety, L. *Langmuir* **2004**, *20*, 11223–11233.
(25) Wang, X. Q.; Rodriguez, J. A.; Hanson, J. C.; Gamarra, D.; Martinez-Arias, A.; Fernandez-Garcia, M. *J. Phys. Chem. B* **2006**, *110*, 428–434.
(26) Saitzek, S.; Villain, S.; Gavarri, J. R. *Adv. Mater. Technol.* **2006**, *513*, 1–14.
(27) Zheng, X. C.; Han, D. Z.; Wang, S. P.; Zhang, S. M.; Wang, S. R.; Haung, W. P.; Wu, S. H. *J. Rare Earths* **2005**, *23*, 47–51.
(28) Bera, P.; Aruna, S. T.; Patil, K. C.; Hegde, M. S. *J. Catal.* **1999**, *186*, 36–44.
(29) Tabakova, T.; Idakiev, V.; Papavasiliou, J.; Avgouropoulos, G.; Ioannides, T. *Catal. Commun.* **2007**, *8*, 101–106.
(30) Delimaris, D.; Ioannides, T. *Appl. Catal. B: Environ.* **2009**, *89*, 295–302.
(31) Ye, X. R.; Jia, D. J.; Yu, J. Q.; Xin, X. Q.; Xue, Z. *Adv. Mater.* **1999**, *11*, 941–942.
(32) Bai, W.; Choy, K. L.; Stelzer, N. H. J.; Schoonman, J. *Solid State Ionics* **1999**, *116*, 225–228.
(33) Bruce, L. A.; Hoang, M.; Hughes, A. E.; Turney, T. W. *Appl. Catal. A: Gen.* **1996**, *134*, 351–362.
(34) Nolan, M.; Verdugo, V. S.; Metiu, H. *Surf. Sci.* **2008**, *602*, 2734–2742.
(35) Yang, Z. X.; Wei, Y. W.; Fu, Z. M.; Lu, Z. S.; Hermansson, K. *Surf. Sci.* **2008**, *602*, 1199–1206.
(36) Pratsinis, S. E. *Prog. Energy Combust. Sci.* **1998**, *24*, 197–219.
(37) Suzuki, M.; Kagawa, M.; Syono, Y.; Hirai, T. *J. Mater. Sci.* **1992**, *27*, 679–684.
(38) Guillou, N.; Nistor, L. C.; Fuess, H.; Hahn, H. *Nanostuct. Mater.* **1997**, *8*, 545–557.
(39) Tschöpe, A.; Ying, J. Y. *Nanostuct. Mater.* **1994**, *4*, 617–623.
(40) Madler, L.; Stark, W. J.; Pratsinis, S. E. *J. Mater. Res.* **2002**, *17*, 1356–1362.
(41) Johannessen, T.; Jenson, J. R.; Mosleh, M.; Johansen, J.; Quaade, U.; Livbjerg, H. *Chem. Eng. Res. Design* **2004**, *82*, 1444–1452.
(42) Feng, X. D.; Sayle, D. C.; Wang, Z. L.; Paras, M. S.; Santora, B.; Sutorik, A. C.; Sayle, T. X. T.; Yang, Y.; Ding, Y.; Wang, X. D.; Her, Y. S. *Science* **2006**, *312*, 1504–1508.
(43) Kim, J. H.; Babushok, V. I.; Germer, T. A.; Mulholland, G. W.; Ehrman, S. H. *J. Mater. Res.* **2003**, *18*, 1614–1622.
(44) Mullins, D. R.; Overbury, S. H.; Huntley, D. R. *Surf. Sci.* **1998**, *409*, 307–319.
(45) Preisler, E. J.; Marsh, O. J.; Beach, R. A.; McGill, T. C. *J. Vac. Sci. Technol. B* **2001**, *19*, 1611–1618.
(46) Frost, D. C.; Ishitani, A.; McDowell, C. A. *Mol. Phys.* **1972**, *24*, 861.
(47) Gao, Y.; Chambers, S. A. *J. Cryst. Growth* **1997**, *174*, 446–454.
(48) Gaskell, K. J.; Starace, A.; Langell, M. A. *J. Phys. Chem. C* **2007**, *111*, 13912–13921.
(49) Tougaard, S. *J. Vac. Sci. Technol. A* **1987**, *5*, 1275–1278.

(50) Samsonov, G. V. *The Oxide Handbook*, 2nd ed.; IFI/Plenum: New York, 1982.
(51) Ehrman, S. H.; Friedlander, S. K.; Zachariah, M. R. *J. Aerosol Sci.* **1998**, *29*, 687–706.
(52) Guo, B.; Kennedy, I. M. *Aerosol Sci. Technol.* **2004**, *38*, 424–436.
(53) Shapovalov, V.; Metiu, H. *J. Catal.* **2007**, *245*, 205–214.
(54) Krummenacher, J. J.; West, K. N.; Schmidt, L. D. *J. Catal.* **2003**, *215*, 332–343.
(55) Li, Y.; Fu, Q.; Flytzani-Stephanopoulos, M. *Appl. Catal. B: Environ.* **2000**, *27*, 179–191.
(56) Clausen, B. S.; Steffensen, G.; Fabius, B.; Villadsen, J.; Feidenhansl, R.; Topsoe, H. *J. Catal.* **1991**, *132*, 524–535.
(57) Rodriguez, J. A.; Hanson, J. C.; Wen, W.; Wang, X. Q.; Brito, J. L.; Martinez-Arias, A.; Fernandez-Garcia, M. *Catal. Today* **2009**, *145*, 188–194.
(58) Wen, W.; Calderon, J. E.; Brito, J. L.; Marinkovic, N.; Hanson, J. C.; Rodriguez, J. A. *J. Phys. Chem. C* **2008**, *112*, 2121–2128.
(59) Djinović, P.; Batista, J.; Pintar, A. *J. Catal. A: Gen.* **2008**, *347*, 23–33.
(60) Arii, T.; Taguchi, T.; Kishi, A.; Ogawa, M.; Sawada, Y. *J. Eur. Ceram. Soc.* **2002**, *22*, 2283–2289.
(61) Kim, C. H.; Bej, S. K.; Thompson, L. T. *Deactivation Mechanisms for Supported Gold Water Gas Shift Catalyst*; Materials Research Society Fall Meeting, Boston, MA, December 2002.
(62) O'Brien, R. J.; Davis, B. H. *Catal. Lett.* **2004**, *94*, 1–6.
(63) Bukur, D. B.; Mukesh, D.; Patel, S. A. *Ind. Eng. Chem. Res.* **1990**, *29*, 194–204.
(64) Rodriguez, J. A.; Liu, P.; Hrbek, J.; Evans, J.; Perez, M. *Angew. Chem., Int. Ed.* **2007**, *46*, 1329–1332.

AM900533P